Anisotropic magnetoresistance across Verwey transition in charge ordered Fe_3O_4 epitaxial films

Xiang Liu,[1] Wenbo Mi,[1,*] Qiang Zhang,[2] and Xixiang Zhang[2,†]

[1]*Tianjin Key Laboratory of Low Dimensional Materials Physics and Preparation Technology, School of Science, Tianjin University, Tianjin 300354, China*

[2]*PSE Division, King Abdullah University of Science and Technology (KAUST), Thuwal 23955-6900, Kingdom of Saudi Arabia*

(Received 10 May 2017; revised manuscript received 20 November 2017; published 26 December 2017)

The anisotropic magnetoresistance (AMR) near the Verwey temperature (T_V) is investigated in charge ordered Fe_3O_4 epitaxial films. When the temperature continuously decreases below T_V, the symmetry of AMR in Fe_3O_4(100) film evolves from twofold to fourfold at a magnetic field of 50 kOe, where the magnetic field is parallel to the film surface, whereas AMR in Fe_3O_4(111) film maintains twofold symmetry. By analyzing AMR below T_V, it is found that the Verwey transition contains two steps, including a fast charge ordering process and a continuous formation process of trimeron, which is comfirmed by the temperature-dependent Raman spectra. Just below T_V, the twofold AMR in Fe_3O_4(100) film originates from uniaxial magnetic anisotropy. The fourfold AMR at a lower temperature can be ascribed to the in-plane trimerons. By comparing the AMR in the films with two orientations, it is found that the trimeron shows a smaller resistivity in a parallel magnetic field. The field-dependent AMR results show that the trimeron-sensitive field has a minimum threshold of about 2 kOe.

DOI: 10.1103/PhysRevB.96.214434

I. INTRODUCTION

Magnetite (Fe_3O_4) with a Curie temperature of 858 K is a mixed valence ferrimagnetic oxide. The tetrahedral (A) sublattice is completely occupied by Fe^{3+} ions, whereas the octahedral (B) sublattice is occupied by an equal number of Fe^{2+} and Fe^{3+} ions. The first principles calculations have shown that only spin-down electrons in the t_{2g} orbit appear at the Fermi level for cubic Fe_3O_4 [1,2]. At 125 K (T_V, the Verwey temperature), Fe_3O_4 undergoes a first-order phase transition called a Verwey transition. Across T_V, the lattice structure of Fe_3O_4 transfers to monoclinic with a Cc space group, where the conductivity drops by more than two orders of magnitude [1–3]. Below T_V, a band gap opens at the Fermi level, and the equivalent Fe_B sites divide into Fe^{2+} and Fe^{3+} in monoclinic Fe_3O_4 [4,5]. Physical properties of Fe_3O_4 also show obvious changes [6–9]. Previous results show that the Fe_3O_4 transport mechanism obeys the small polaron (SP) hopping model above 200 K and the band gap model below 200 K [10]. Both band gap and variable-range hopping (VRH) models can fit the resistivity-temperature (ρ-T) curve at $T < T_V$ [10]. Although the Verwey transition has been observed for nearly 80 years, its mechanism is still debated. Recently, Senn *et al.* [11,12] have found that the bond length of Fe_B^{2+}-Fe_B^{3+} shows a wide distribution below T_V. The anomalous shortage of some Fe_B^{3+}-Fe_B^{2+}-Fe_B^{3+} chains suggests that the spin-down t_{2g} electron at Fe_B^{2+} is localized in the three-Fe-site unit called a trimeron, which is different from the previous dimerization model [13]. The novel microstructure may provide a way to understand the Verwey transition.

The investigation of magnetotransport behavior across T_V in Fe_3O_4 is very important to clarifying the Verwey transition. The anisotropic magnetoresistance (AMR) of Fe_3O_4 is one of the special magnetotransport properties and is a result of the spin-orbital coupling effect [14–16]. In ferromagnets, the configuration of spin-up and spin-down electrons results in magnetization-direction-dependent resistivity. The spin direction tends to align parallel to the easy axis, where AMR depends on the easy axis direction which, however, can be affected by the shape anisotropy or strain. The easy axis of bulk Fe_3O_4 is along $\langle 111\rangle_c$ above 130 K and $[001]_c$ below 130 K, where the symmetry of magnetic anisotropy turns from cubic to uniaxial [17,18]. Thus, below T_V, AMR in a single-phase monoclinic Fe_3O_4 should possess twofold symmetry in accordance with the uniaxial magnetocrystalline anisotropy (MCA). However, AMR shows fourfold symmetry in Fe_3O_4(100) films below T_V [19–21]. The contradiction between uniaxial magnetic anisotropy and fourfold AMR must necessarily be clarified. Furthermore, the relation between charge ordering and AMR is also an open question. Here, AMR across T_V in high-quality epitaxial Fe_3O_4 films with different orientations is investigated systematically. Remarkably, AMR turns from twofold to fourfold symmetry in Fe_3O_4(100) film below T_V. We propose that trimerons [11,12] play an important role in fourfold AMR below T_V.

II. EXPERIMENT

Epitaxial Fe_3O_4 films with different orientations were fabricated on MgO(100) and Al_2O_3(0001) substrates by a dc magnetron sputtering apparatus from a pure Fe (99.99%) target. When the base pressure of the chamber was lower than 6.0×10^{-8} Torr, Ar (99.999%) and O_2 (99.999%) gas mixture was introduced into the chamber to 8 mTorr with a mixing ratio of Ar:O_2 = 10:0.7. The sputtering power on the Fe target was 150 W. The substrate temperature was kept at 700 °C during sputtering. The film thickness was 200 nm as determined by a Dektak 6M surface profiler and transition electron microscopy (TEM). The microstructure of Fe_3O_4 films was characterized by high-resolution transmission electron microscopy (HRTEM), where the focused ion beam etching was used to prepare the samples for TEM observation. The electronic transport properties of Fe_3O_4 films were measured in the temperature range from 2 to 300 K by

*Corresponding author: miwenbo@tju.edu.cn
*Corresponding author: xixiang.zhang@kaust.edu.sa

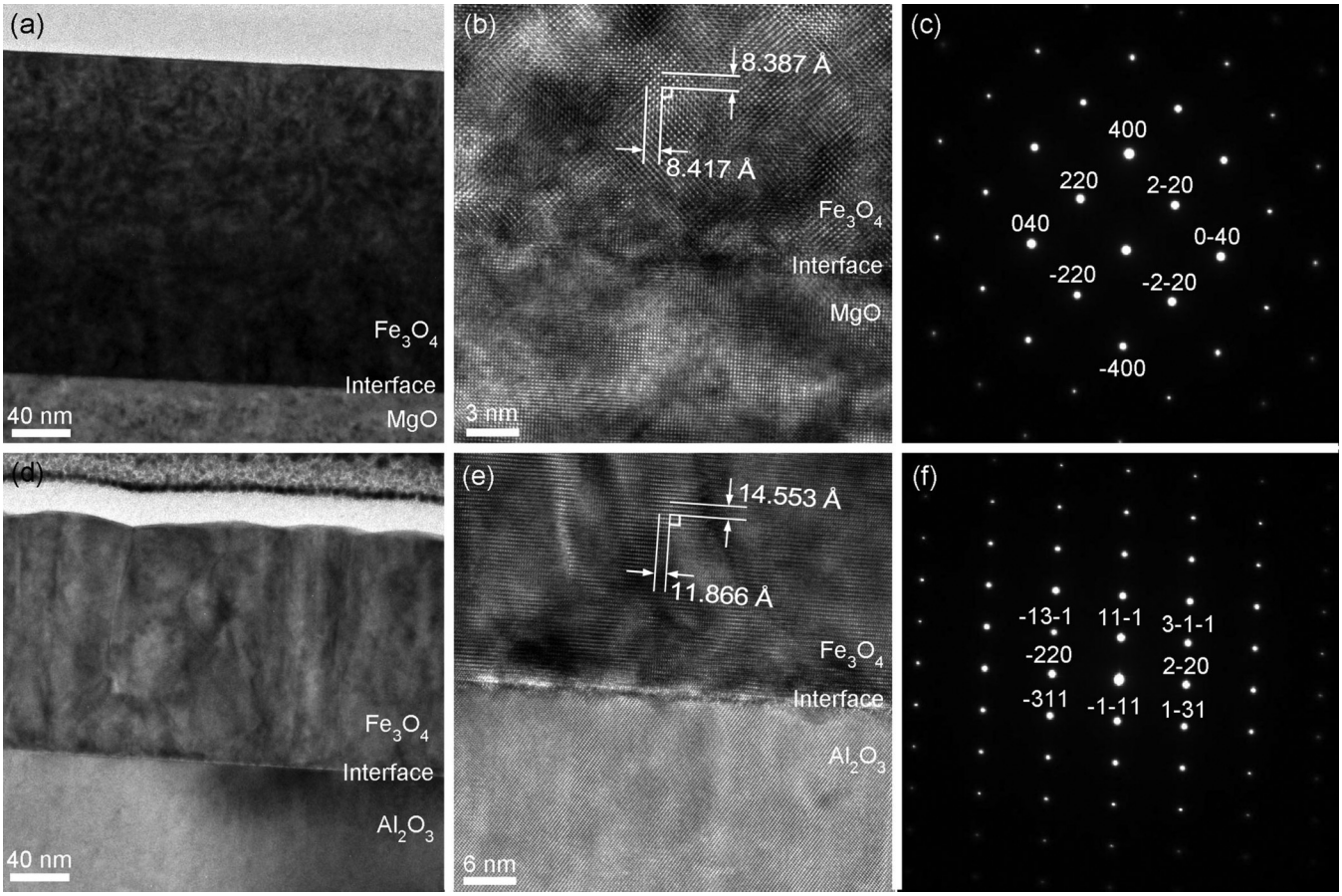

FIG. 1. Low-magnification, high-resolution TEM images and SAED patterns of epitaxial Fe_3O_4 films on MgO(100) (a–c) and Al_2O_3(0001) (d–f) substrates.

Quantum Design physical property measurement system, and the magnetic properties were measured by a Quantum Design superconducting quantum interference device (SQUID).

III. RESULTS AND DISCUSSION

A. Crystal structure

Figure 1 shows the TEM images and selected area electronic diffraction (SAED) patterns of Fe_3O_4(100) [Fig. 1(a)–1(c)] and (111) [Fig. 1(d)–1(f)] films on MgO(100) and Al_2O_3(0001) substrates, respectively. The low-magnification TEM images in Figs. 1(a) and 1(d) show the sharp interfaces and thicknesses of the Fe_3O_4(100) and (111) films. In Figs. 1(b) and 1(e), HRTEM images show the epitaxial growth of Fe_3O_4 films with a sharp interface. The out-of-plane and in-plane lattice constants are 8.387 and 8.417 Å of Fe_3O_4(100) film and 14.553 and 11.866 Å of Fe_3O_4(111) film along the [111] and [110] directions. The lattice constant of bulk Fe_3O_4 is 8.396 Å [22]. The discrepancy of the lattice constant between films and bulk is less than 0.3%, which can be ascribed to weak strain. In Figs. 1(c) and 1(f), the SAED patterns further reveal the epitaxial structure of Fe_3O_4(100) and (111) films. The unique group of SAED patterns of each sample suggests that the lattice of Fe_3O_4 films matches that of substrates well. The electron microscopic results confirm the high-quality epitaxial growth of Fe_3O_4(100) and (111) films.

Figures 2(a) and 2(b) show the temperature-dependent Raman spectra of Fe_3O_4(100) and (111) films at temperatures ranging from 140 to 80 K. Previous results have shown that five Raman-activated modes ($A_{1g} + E_g + 3T_{2g}$) appear above T_V, but 78 modes ($23A_g + 24B_{1g} + 16B_{2g} + 15B_{3g}$) occur below T_V [23,24]. Raman-activated modes of E_g, $T_{2g}(2)$, and A_{1g} are observed in the entire temperature range, where a blueshift appears in both films with the decrease of temperature. The Raman spectra of Fe_3O_4(100) film above 100 K and that of Fe_3O_4(111) film above 110 K show no obvious changes. However, some peaks at 165, 203, 342, 382, and 468 cm^{-1} distinct from the five cubic Raman modes gradually appear in Fe_3O_4(100) film below 100 K and in Fe_3O_4(111) film below 110 K, showing the occurrence of ionic displacement. Below T_V, Raman-active modes appear around 166, 203, 324, 343, 363, 382, 412, 471, 548, 622, and 675 cm^{-1}.

B. Magnetic properties

Figures 3(a) and 3(b) show the temperature-dependent resistivity/magnetization of Fe_3O_4(100) and (111) films, respectively. The abrupt increase (decrease) of resistivity (magnetization) can be ascribed to the Verwey transition. In Figs. 3(a) and 3(b), the magnetization of Fe_3O_4 films shows a well-known dependence on temperature. An in-plane 100-Oe field was applied during magnetization-temperature (M-T) measurements. The magnetization first increases as

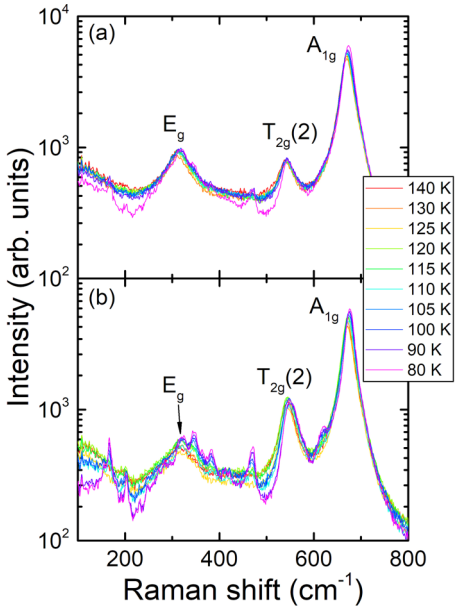

FIG. 2. Temperature-dependent Raman spectra of (a) Fe_3O_4(100) film and (b) Fe_3O_4(111) film.

temperature decreases from room temperature because the negative MCA constant K_1 of Fe_3O_4 increases with a decrease in temperature [18], thus making it easier to magnetize Fe_3O_4. At T_V, the magnetization shows a sharp decrease. Previous results revealed that the anomalous reduction of magnetization results from a spontaneous MCA [25]. Below T_V, the easy axis turns to $[001]_m$ [18]. The monoclinic Cc structure can form up to 24 orientations with six equal probabilities of c axis orientation during zero-field cooling [26,27]. When the magnetic field is along one of the cubic ⟨001⟩ directions, the c axis can be aligned during field cooling above 1000 Oe [26]. Below T_V, only about one-third of c axes are along the field direction in Fe_3O_4(100) films and no easy axis is along the field direction in Fe_3O_4(111) films under the low field measurements. The applied magnetic field is lower than the coercive field of monoclinic Fe_3O_4. Hence, Fe_3O_4 is difficult to magnetize below T_V, which results in the abrupt decrease of magnetization across T_V.

C. Transport properties

In Fe_3O_4(100) and (111) films, the transition temperature, which is defined by the maximum slope of log ρ, is 118 and 125 K, respectively. Several factors, including stoichiometry, residual strain, difference in thermal expansion coefficients between substrates and Fe_3O_4 films, and antiphase boundaries (APBs) can affect the Verwey transition [22,28–31]. First, in Fig. 4, Rutherford backscattering spectrometry is investigated to determine the stoichiometry of Fe_3O_4 films on Si substrate, which is simultaneously fabricated with Fe_3O_4(100) and (111) epitaxial films. In Fig. 4(b), the atomic fraction of Fe and O in Fe_3O_4 film is 42.8571% and 57.1429%, respectively. The Fe-(O-)fraction shows fluctuation at the interface because of the diffusion of Fe_3O_4 and oxidation of the Si substrate. The discrepancy $\delta \approx 1.75 \times 10^{-6}$ of $Fe_{3(1-\delta)}O_4$ reveals a nearly exact stoichiometry. Then, the strain from the different thermal expansion coefficients between the substrates and Fe_3O_4 film was estimated. We simply assumed that the thermal expansion coefficient is temperature independent [32]. As temperature decreases from 300 to 120 K, the strain in Fe_3O_4(100) film changes from 0.33% to 0.38%; the strain in Fe_3O_4(111) film changes from 0.26% to 0.33%, in theory. Although the strain change is less than 0.07%, the thermal expansion coefficient between film and substrates is a possible reason for the different transition temperature [29]. Besides, although the influence of different strain due to the lattice mismatch in

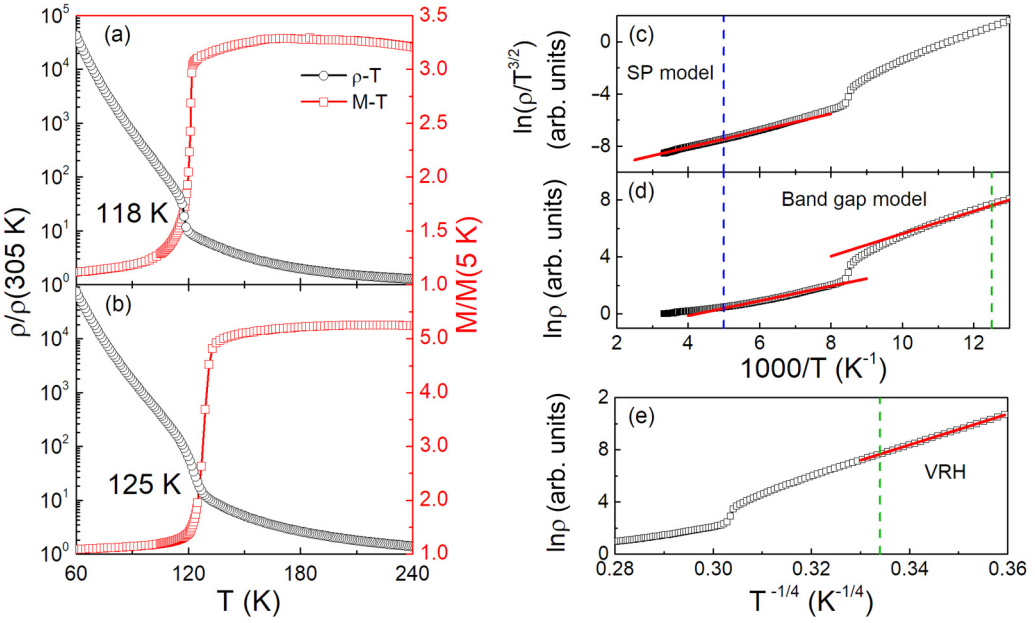

FIG. 3. Temperature-dependent resistivity/magnetization of epitaxial Fe_3O_4 films on (a) MgO(100) and (b) Al_2O_3(0001) substrates. ρ-T dependence of Fe_3O_4(100) film in different temperature ranges fitted by (c) small polaron model, (d) band gap model, and (e) variable-range hopping model. Blue and green dashed lines (c–e) indicate 200 K and 80 K, respectively.

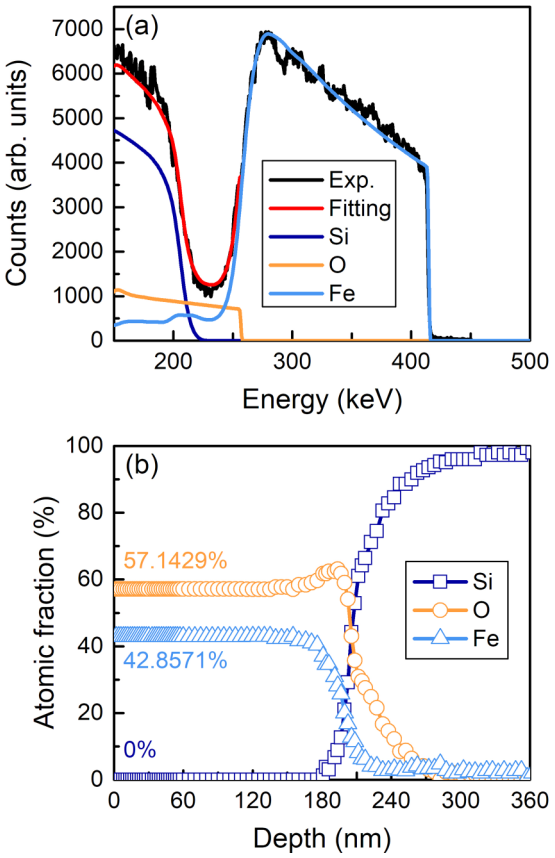

FIG. 4. (a) RBS profiles of Fe_3O_4 film on Si substrate; (b) the composition versus penetration depth of the same sample.

Fe_3O_4(100) and (111) films is weak, it is still a possible factor that cannot be excluded. Last but not least, APBs in Fe_3O_4 are an important factor of the Verwey transition. As Wright *et al.* [33] proposed, the long-range order of Fe^{2+} and Fe^{3+} ions at octahedral sites is necessary for the Verwey transition. However, the antiphase boundaries formed during Fe_3O_4 film deposition on MgO and Al_2O_3 substrates inhibit the long-range order [34]. The difference in antiphase domain size between Fe_3O_4(100) and (111) films [35] may be the reason for the different T_V. Thus, the different T_V of the samples may be ascribed to the APBs in Fe_3O_4 films and the different strain magnitudes from the different thermal expansion coefficients or lattice mismatch between films and substrates.

The ρ-T dependence indicates the transport mechanism in Fe_3O_4. Above T_V, the ρ-T curve is fitted by the SP model $[\rho/T^{3/2} = A\exp(W_p/k_BT)]$ at $T > 200$ K [Fig. 3(c)]. Meanwhile, it is also be fitted by band gap model $[\rho = \rho_\infty \exp(E_a/k_BT)]$ at $T_V < T < 200$ K [Fig. 3(d)], where A is a pre-exponential factor, W_p and E_a represent the polaron hopping energy and activation energy, and k_B is the Boltzmann constant. Ihle *and* Lorenz [36] pointed out that the conductivity in Fe_3O_4 consists of SP band conductivity and SP hopping conductivity at $T_1 < T < 500$ K, where $T_1 \approx T_V/2$, while the transport mechanism obeys the Mott VRH model below T_1. The carrier in Fe_3O_4 is the spin-down electron in the t_{2g} orbital, which can be regarded as SP with a large effective mass due to Jahn-Teller distortion around Fe_B^{2+} sites [37–39]. For SP band conductivity, the thermal activation of carriers between the nearest neighbor sites contributes to the conduction, where the phonon localizes and does not participate in the electronic hopping. For SP hopping conductivity, the conduction is SP hopping, which is accompanied by multiphonon absorptions and emissions [36]. Above 200 K, SP hopping is the main conductive mechanism, while at $T_V < T < 200$ K, the transport mechanism is dominated by SP band conductivity because the energy is not enough to make phonon transport between Fe_B sites. With the decrease of temperature, the short-range polaronic order develops. The development process follows Arrhenius behavior. Table I lists W_p and E_a of both samples, where W_p is greater than E_a above T_V, revealing that only a higher temperature can sustain SP hopping together with the change of phonon. Around T_V, the Verwey transition (long-range order) is destructed, and the polaronic order (short-range order) at the Fe_B sites is diminished, but the band gap does not collapse with the increase of temperature. Strong electron-phonon coupling causes the pseudogaplike behavior at the Fermi level [40]. Photoemission spectroscopy results show that the activation energy reduces from 150 to 100 meV on heating through T_V. The reduction of activation energy results in a jump of conductivity by a factor of 125 at T_V, which is consistent with the two orders of magnitude resistivity jump in bulk Fe_3O_4 [41]. Below T_V, the transport mechanism is more intricate. Several studies fitted the ρ-T curve using the VRH model above T_V but show a deviation at 80 K $< T < T_V$ [42,43]. We used both band gap model and VRH models $[\rho = \rho_\infty \exp(T_0/T)^{1/4}]$ to fit the curve above T_V. A band gap model was used in different ranges of $1000/T$, including $10 \sim 12.5$, $10 \sim 16$, $9 \sim 12.5$, and $9 \sim 16\,K^{-1}$, where the range of $10\,K^{-1} < 1000/T < 12.5\,K^{-1}$ shows the lowest residual sum of squares. In Fig. 3(e), the ρ-T curve fitted by the VRH model below 80 K is shown. The fitted Mott temperature (T_0) is listed in Table I. Both the band gap and VRH models give reasonable fit results, which leads to an ambiguity of transport mechanism for Fe_3O_4 below T_V. Nevertheless, it is no doubt that the conductivity still derives from the hopping of the spin-down t_{2g} electron along Fe^{2+}-Fe^{3+}, even at such low temperatures.

TABLE I. Values of polaron hopping energy (W_p), activation energy (E_a), and Mott temperature (T_0) of Fe_3O_4(100) and (111) films obtained by different transport models at different temperature ranges.

	SP hopping	Band gap model (meV)		
Orientations	(meV) W_p	$E_a(T_V < T < 200\,K)$	$E_a(60\,K < T < T_V)$	VRH (K) T_0
(100)	55.4	44.9	68.3	2.0×10^8
(111)	66.8	54.3	77.3	1.5×10^8

Figure 5 shows the AMR dependence on the temperature and magnetic field of Fe_3O_4(100) film. Here, AMR is defined as $\text{AMR} = (\rho_\varphi - \rho_{180^\circ})/\rho_{180^\circ} \times 100\%$, where φ is the angle between the magnetic field and current. We set $\varphi = 0$ for the magnetic field perpendicular to the current. In Fig. 5(a), the temperature-dependent AMR is detected at a magnetic field of 50 kOe. The AMR symmetry shows a transition from

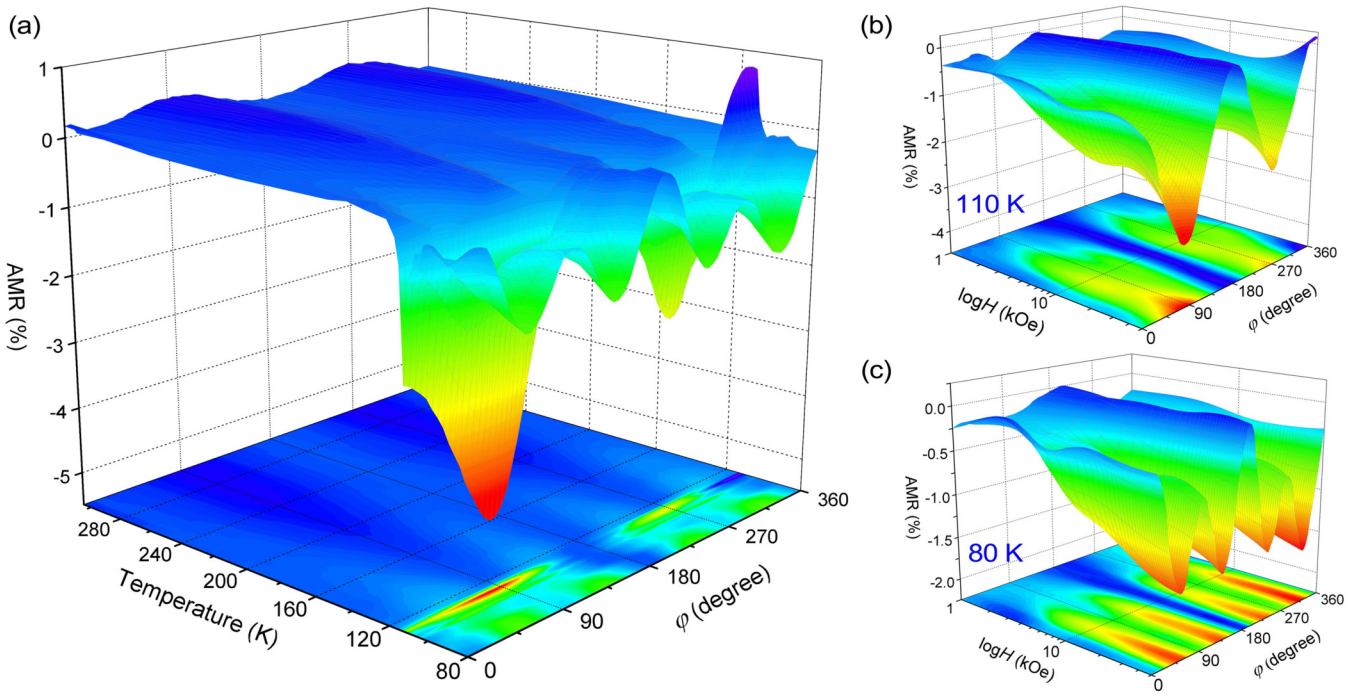

FIG. 5. AMR measured in Fe_3O_4(100) film. (a) Temperature-dependent AMR at a 50-kOe magnetic field. (b,c) Field-dependent AMR at 110 K and 80 K, respectively.

twofold to fourfold, followed by a sign change at 200 K. When the temperature cools down to 114 K, AMR shows twofold symmetry again and the maximum value of −4.5% at 112 K. At $T \leqslant 104$ K, AMR gradually turns to fourfold symmetry within 10 K and maintains fourfold symmetry at $T < 80$ K. Figures 5(b) and 5(c) show the magnetic field dependence of AMR at 110 and 80 K, respectively. At 110 K, AMR almost maintains twofold symmetry but shows a bit of broadening at 5 kOe $\leqslant H \leqslant$ 10 kOe due to weak fourfold symmetry. At 80 K, twofold AMR transforms to fourfold when the magnetic field is larger than 2 kOe.

The AMR curves of the Fe_3O_4(111) film were also measured to further investigate the lattice orientation effects. In Fig. 6(a), AMR maintains twofold symmetry at a 50-kOe magnetic field from 80 to 305 K. At $T > 128$ K, the AMR of Fe_3O_4(111) film is less than −0.5%, which is almost temperature independent. The maximum AMR of −4.2% appears at 120 K. Figures 6(b) and 6(c) show the magnetic-field-dependent AMR at 110 and 80 K, respectively. At 110 K, sixfoldlike AMR appears at 2 kOe $\leqslant H \leqslant$ 20 kOe. The maxima of AMR for Fe_3O_4(111) film appear at $\varphi =$ 60°,120°,240°, and 300° rather than 45°, 135°, 225°, and 315°. The AMR peaks are broadened at $H > 20$ kOe and finally turns into twofold at a 50-kOe magnetic field. At 80 K, AMR almost maintains twofold symmetry but broadens at 5 kOe $\leqslant H \leqslant$ 20 kOe due to sixfold symmetry.

The easy axis of bulk Fe_3O_4 is along the ⟨111⟩ direction at high temperatures [17]. In Fe_3O_4(100) film, the easy axis projects onto the in-plane ⟨110⟩ direction because of shape anisotropy [19]. Thus, AMR symmetry in the Fe_3O_4(100) film should be fourfold due to the fourfold in-plane MCA above T_V [19]. The experimental results of Fe_3O_4(100) film are consistent with the analyses at $T_V < T < 200$ K, but contradictory at $T > 200$ K. Several experiments [10,20] have observed the AMR transition in Fe_3O_4 bulk and film across 200 K. However, the origin of the AMR transition is still unclear. The different transport mechanisms across 200 K may play an important role in AMR transition [10]. In Fe_3O_4(111) film, the easy axis is along the out-of-plane ⟨111⟩ direction [19]. The AMR shows twofold symmetry according to the resistivity tensor, which is consistent with the experimental results at $T > T_V$.

In Fe_3O_4(100) film, AMR shows a continuous change with the decrease of temperature below 116 K. Some electronic microscopic results have shown that the monoclinic c axis can be selected from the three equivalent $\langle 001 \rangle_c$ directions during field cooling [18,27,44]. In Fig. 7(a), the monoclinic c axis in our Fe_3O_4(100) film is along $[100]_c$. The monoclinic a and b axes are equally divided by the surface normal. Therefore, AMR exhibits twofold symmetry at 104 K $< T <$ 116 K due to uniaxial MCA [Fig. 5(a)]. In Fig. 5(b), the positive magnetic field dependence of AMR also indicates that the twofold AMR depends on MCA. However, the fourfold AMR appears at $T \leqslant 104$ K. The sharp jump in the ρ-T curve manifests that the AMR transition below 104 K does not derive from charge ordering, so we consider the transition contains two processes. At the first step, the charge ordering takes place together with the cubic-monoclinic transition when the temperature is just below T_V (A process). The AMR shows twofold symmetry at the first sharp step due of the uniaxial MCA. Process A is followed by a continuous formation of trimeron denoted as the B process. Process B proceeds until trimerons spread all over the film at a lower temperature. Correspondingly, as explained below, the fourfold item gradually becomes visible at $T \leqslant 104$ K. In view of the temperature-dependent Raman spectra, the Raman-activated modes of monoclinic Fe_3O_4

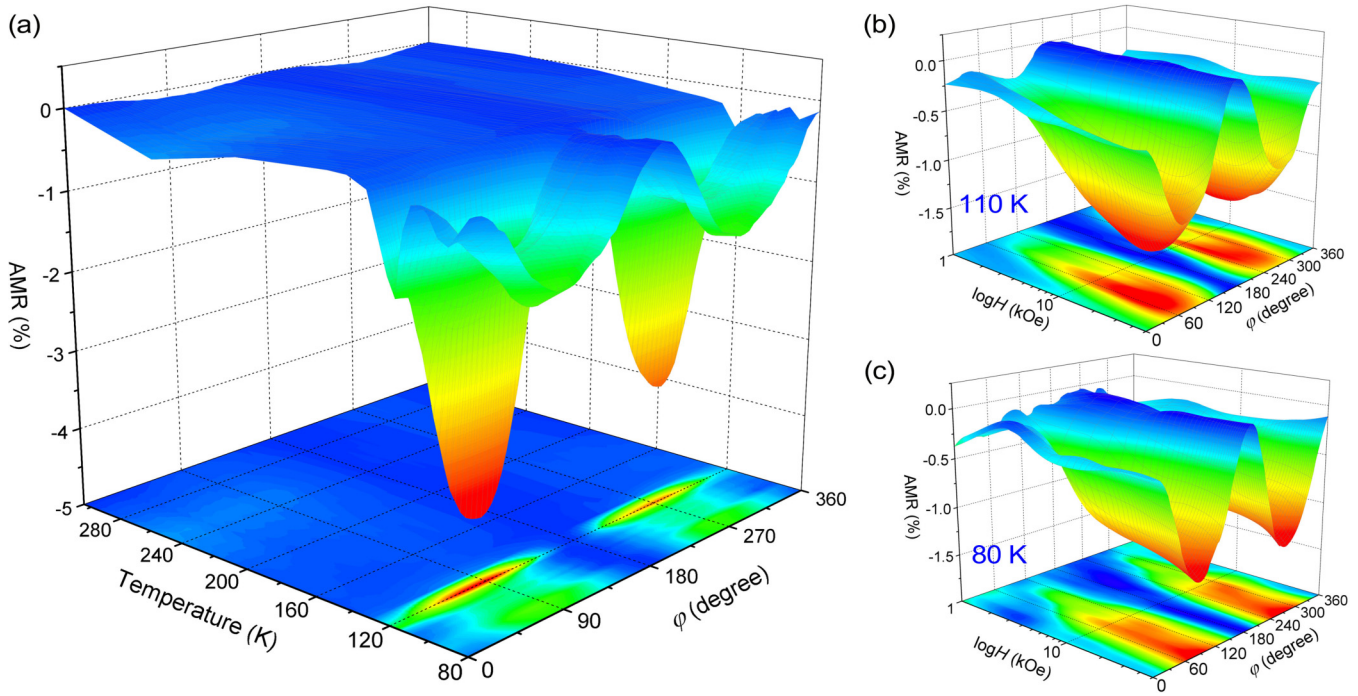

FIG. 6. AMR of $Fe_3O_4(111)$ film. (a) Temperature-dependent AMR at a 50-kOe magnetic field. (b,c) Field-dependent AMR at 110 K and 80 K, respectively.

gradually appear at $T < T_V - 15\,K$, revealing a temperature gap between charge ordering and lattice distortion. It is noted that although the lattice does not distort just below T_V, the inequivalent Fe^{2+} and Fe^{3+} ions at Fe_B sites have to be described by a monoclinic space group. Thus, the A process contains the cubic-monoclinic transition.

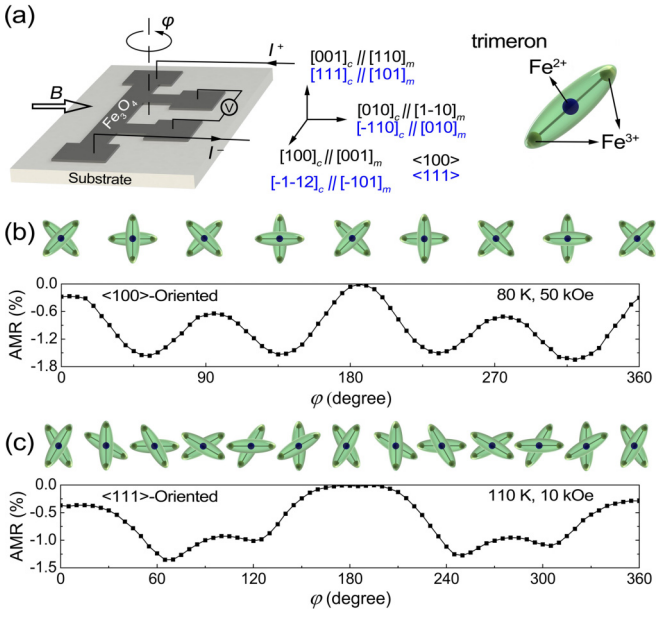

FIG. 7. (a) Sketch map of the sample, magnetic field, and current arrangement used in our work. (b) AMR at 80 K and 50 kOe of $Fe_3O_4(100)$ film and the in-plane trimerons distribution at the corresponding angle. (c) AMR at 110 K and 10 kOe of $Fe_3O_4(111)$ film and the in-plane trimeron distribution at the corresponding angle. The structure of the trimeron is shown in the upper right corner.

In order to clarify the effects of the trimeron on the AMR, the distributions of trimerons in $Fe_3O_4(100)$ and (111) films were compared. It is noted that we only consider the in-plane trimerons. In $Fe_3O_4(100)$ film, the in-plane trimerons are along $[1-11]_m$ and $[-111]_m$. In Fig. 7(b), the top view of the in-plane trimerons distribution with the corresponding φ shows fourfold symmetry. The AMR maximum appears at $\varphi = 45°, 135°, 225°$, and $315°$. Simultaneously, the trimerons are parallel or perpendicular to the magnetic field. In $Fe_3O_4(111)$ film, the in-plane trimerons are along $[010]_m$, $[11-1]_m$ and $[-111]_m$, which has sixfold symmetry, while the trimerons along $[010]_m$ are considered to be irrelevant to AMR because the Fe^{3+}-Fe^{2+}-Fe^{3+} chains are perpendicular to the electronic transport direction. In Fig. 7(c), the in-plane trimerons show twofold symmetry without $[010]_m$. The AMR maximum in $Fe_3O_4(111)$ film appears at 60°, 120°, 240°, and 300°, where one of the in-plane trimerons is parallel to the magnetic field. Together with Fig. 7(b), the AMR maximum appears when the magnetic field is parallel to the in-plane trimerons. In other words, the trimerons can be activated with a smaller resistivity by a parallel magnetic field [45]. In Figs. 5(c), 6(b), and 6(c), the appearance of twofold AMR under a low field reveals that the external activated field has a threshold of about 2 kOe. It is interesting that the sixfoldlike AMR in the $Fe_3O_4(111)$ film only appears at a middle field, while in Figs. 6(b) and 6(c), the AMR shows twofold symmetry under a high magnetic field. We wonder whether magnetic anisotropy exists in a trimeron where the "easy axis" is along a trimeron. Hence, the trimeron has a smaller resistivity when the spin direction is along the trimeron due to the parallel magnetic field. In the $Fe_3O_4(111)$ film, the electronic transport is frustrated

TABLE II. The number of trimerons along specific monoclinic crystal orientations at different azimuth angles.

Crystal orientations	0°	45°
$[100]_m$	4	4
$[010]_m$	8	8
$[001]_m$	0	20
$[111]_m$	6	6
$[-111]_m$	4	4
$[1-11]_m$	6	6
$[-1-11]_m$	4	4

with a smaller conductivity owing to the low nonparallel magnetic field at $\varphi = 90^\circ$ and 270°. At $H > 20$ kOe, AMR becomes twofold, confirming that the external magnetic field has more influence on trimerons of both the sides. The resultant conductivity of trimerons reduces the total resistivity. On the other hand, the resultant properties of $Fe_3O_4(100)$ film are not prominent because of the large included angle between trimerons. By considering the dependence of a monoclinic c axis on the cooling field direction [26], the angle between the trimeron-sensitive field and the trimeron should have a maximum in the range of $30^\circ \sim 45^\circ$. It is consistent with our proposal that only in-plane trimerons are considered. In order to verify our speculation on the magnetic anisotropy in the trimeron, the distribution of trimerons in the monoclinic Cc unit cell was counted. In Table II, all of the trimerons are along several specific lattice orientations, including $[100]_m$, $[010]_m$, $[111]_m$, $[-111]_m$, $[1-11]_m$, and $[-1-11]_m$. There is an azimuth angle between the trimeron and a specific crystal axis. The anisotropy of trimerons is considered to contribute to the specific crystal axis if the azimuth angle is less than 45°. Based on this speculation, the number of trimerons whose anisotropy contributes to the $[001]_m$ axis increases to 20. However, the number shows no change along other orientations. The decreased number of trimerons along $[001]_m$, $[010]_m$, and $[100]_m$ is in good agreement with the experimental results on MCA, where the easy, intermediate, and hard axes are along $[001]_m$, $[010]_m$, and $[100]_m$, respectively [46,47]. We also performed the simulations on the magnetic anisotropy energy of monoclinic Fe_3O_4 by density functional theory. The calculation details have been published elsewhere [5]. Spin-orbital coupling is considered to describe the spin configuration. The direct calculations on anisotropy of trimerons are limited, so we compared the total energy of monoclinic Fe_3O_4 with spin direction along $[001]_m$, $[010]_m$, and $[100]_m$. We assumed that the total anisotropy derives from trimerons because (1) all of the Fe_A sites are trivalent whose $3d$ orbitals are half-filled. The anisotropy of Fe_A sites can be neglected. (2) Only several Fe_B sites with trivalent states do not participant in the trimeron, whose anisotropy can be neglected, as well. The anisotropy of the trimeron could be described with a uniaxial anisotropic model since a trimeron is a one-dimension ionic chain. The magnetocrystalline anisotropy energy can be expressed as

$$E = \sum_i n_i K_1 \sin^2\theta_i + \sum_i n_i K_2 \sin^4\theta_i, \quad (1)$$

where K_1 and K_2 are the anisotropic constants of a single trimeron, n is the number of trimerons along a specific direction, and θ is the angle between magnetization and the trimeron. Our results were

$$\begin{aligned} &[001]: -1564.4343\,\text{eV} = 22VK_1 + 17VK_2 + E_0 \\ &[010]: -1564.4339\,\text{eV} = 19VK_1 + 15.25VK_2 + E_0 \\ &[100]: -1564.4317\,\text{eV} = 23VK_1 + 19.25VK_2 + E_0 \\ &\Rightarrow \begin{cases} K_1 = -7.35 \times 10^5 \text{erg/cm}^3 \\ K_2 = 11.06 \times 10^5 \text{erg/cm}^3 \end{cases}, \end{aligned} \quad (2)$$

which reveals the anisotropy of the trimeron. Fe_A-Fe_B is still coupled with the superexchange interaction based on the calculations, although the trimeron shows obvious anisotropy.

The effect of APBs on AMR was also considered. Electron microscopic studies have shown that the in-plane APBs have fourfold symmetry in $Fe_3O_4(100)$ film [48]. However, just below T_V, the AMR of $Fe_3O_4(100)$ film maintains twofold symmetry, revealing that the fourfold APBs are invalid to AMR. Furthermore, Hu *et al.* [21] reported that AMR in the cross-sectional plane of $Fe_3O_4(100)$ film shows fourfold symmetry [21], which can rule out the effect of APBs.

IV. CONCLUSION

The AMR of high-quality epitaxial Fe_3O_4 films on MgO(100) and $Al_2O_3(0001)$ substrates was investigated systematically. It was found that the Verwey transition contains two processes, including a fast charge ordering process and a continuous formation of trimeron process. In $Fe_3O_4(100)$ film, the twofold AMR at $104\,\text{K} < T < 116\,\text{K}$ comes from the uniaxial magnetic anisotropy, whereas the fourfold AMR at $T \leqslant 104$ K can be ascribed to the in-plane trimerons. By comparing the AMR below T_V between two oriented films, it shows the maxima when trimerons are parallel to the magnetic field. A uniaxial magnetic anisotropy might appear in the trimeron, and the easy axis is along the trimeron. Experimental results indicate that the magnetic field $H > 2$ kOe approximately parallel to the axis of trimeron may induce a smaller resistivity. The in-plane trimerons play an important role in the complex AMR behavior below T_V. However, the sign and symmetry change of AMR in $Fe_3O_4(100)$ film at 200 K remains a mystery. Further investigations are needed to reveal the origin of the anomalous AMR behavior.

ACKNOWLEDGMENTS

This work is supported by the National Natural Science Foundation of China (Grants No. 51671142 and No. U1632152) and the Key Project of the Natural Science Foundation of Tianjin (Grant No. 16JCZDJC37300).

[1] Z. Zhang and S. Satpathy, Phys. Rev. B **44**, 13319 (1991).
[2] Y. Yanase and K. Siratori, J. Phys. Soc. Jpn. **53**, 312 (1984).
[3] J. E. W. Verwey and P. W. Haayman, Physica **8**, 979 (1941).
[4] H. T. Jeng, G. Y. Guo, and D. J. Huang, Phys. Rev. Lett. **93**, 156403 (2004).
[5] X. Liu, L. Yin, and W. B. Mi, Sci. Rep. **7**, 43403 (2017).
[6] P. Weiss and R. Forrer, Ann. Phys. **10**, 279 (1929).
[7] R. W. Millar, J. Am. Chem. Soc. **51**, 215 (1929).
[8] E. J. Verwey, Nature **144**, 327 (1939).
[9] L. R. Bickford, Rev. Mod. Phys. **25**, 75 (1953).
[10] R. Ramos, S. K. Arora, and I. V. Shvets, Phys. Rev. B **78**, 214402 (2008).
[11] M. S. Senn, J. P. Wright, and J. P. Attfield, Nature **481**, 173 (2012).
[12] M. S. Senn, I. Loa, J. P. Wright, and J. P. Attfield, Phys. Rev. B **85**, 125119 (2012).
[13] P. W. Anderson, Phys. Rev. **102**, 1008 (1956).
[14] J. Smit, Physica (Amsterdam) **17**, 612 (1951).
[15] T. R. McGuire and R. I. Potter, IEEE Trans. Magn. **11**, 1018 (1975).
[16] J. P. Jan, in *Solid State Physics*, edited by F. Seitz and D. Turnbull, Vol. 5 (Academic, New York, 1957), p. 1.
[17] L. R. Bickford, Phys. Rev. **76**, 137 (1949).
[18] L. R. Bickford, Phys. Rev. **78**, 449 (1950).
[19] P. Li, E. Y. Jiang, and H. L. Bai, Appl. Phys. Lett. **96**, 092502 (2010).
[20] P. Li, C. Jin, E. Y. Jiang, and H. L. Bai, J. Appl. Phys. **108**, 093921 (2010).
[21] C. R. Hu, J. Zhu, G. Chen, J. X. Li, and Y. Z. Wu, Phys. Lett. A **376**, 3317 (2012).
[22] W. F. J. Fontijn, R. M. Wolf, R. Metselaar, and P. J. van der Zaag, Thin Solid Films **292**, 270 (1997).
[23] L. V. Gasparov, D. B. Tanner, D. B. Romero, H. Berger, G. Margaritondo, and L. Forro, Phys. Rev. B **62**, 7939 (2000).
[24] O. N. Shebanova and P. Lazor, J. Solid State Chem. **174**, 424 (2003).
[25] F. Walz, J. Phys.: Condens. Matter **14**, R285 (2002).
[26] B. A. Calhoun, Phys. Rev. **94**, 1577 (1954).
[27] T. Kasama, R. J. Harrison, N. S. Church, M. Nagao, J. M. Feinberg, and R. E. Dunin-Borkowski, Phase Transitions **86**, 67 (2013).
[28] J. P. Shepherd, J. W. Koenitzer, R. Aragón, J. Spałek, and J. M. Honig, Phys. Rev. B **43**, 8461 (1991).
[29] P. J. van der Zaag, W. F. J. Fontijn, P. Gaspard, R. M. Wolf, V. A. M. Brabers, R. J. M. van de Veerdonk, and P. A. A. van der Heijden, J. Appl. Phys. **79**, 5936 (1996).
[30] W. F. J. Fontijn, P. A. A. van der Heijden, F. C. Voogt, T. Hibma, and P. J. van der Zaag, J. Magn. Magn. Mater. **165**, 401 (1997).
[31] W. Eerenstein, T. T. M. Palstra, T. Hibma, and S. Celotto, Phys. Rev. B **66**, 201101 (2002).
[32] J. S. Y. Feng and M. A. Nicolet, J. Phys. Chem. Solids **36**, 835 (1975).
[33] J. P. Wright, J. P. Attfield, and P. G. Radaelli, Phys. Rev. Lett. **87**, 266401 (2001).
[34] J. B. Moussy, S. Gota, A. Bataille, M. J. Guittet, M. Gautier-Soyer, F. Delille, B. Dieny, F. Ott, T. D. Doan, P. Warin, P. Bayle-Guillemaud, C. Gatel, and E. Snoeck, Phys. Rev. B **70**, 174448 (2004).
[35] S. M. Thompson, V. K. Lazarov, R. C. Bradley, T. Deakin, B. Kaeswurm, G. E. Sterbinsky, J. Cheng, and B. W. Wessels, J. Appl. Phys. **107**, 09B102 (2010).
[36] D. Ihle and B. Lorenz, J. Phys. C **19**, 5239 (1986).
[37] J. P. Wright, J. P. Attfield, and P. G. Radaelli, Phys. Rev. B **66**, 214422 (2002).
[38] H. J. Pinto and S. D. Elliott, J. Phys.: Condens. Matter **18**, 10427 (2006).
[39] F. Zhou and G. Ceder, Phys. Rev. B **81**, 205113 (2010).
[40] S. K. Park, T. Ishikawa, and Y. Tokura, Phys. Rev. B **58**, 3717 (1998).
[41] J. H. Park, L. H. Tjeng, J. W. Allen, P. Metcalf, and C. T. Chen, Phys. Rev. B **55**, 12813 (1997).
[42] J. R. Drabble, T. D. Whyte, and R. M. Hooper, Solid State Commun. **9**, 275 (1971).
[43] H. Graener, M. Rosenberg, T. E. Whall, and M. R. B. Jones, Philos. Mag. B **40**, 389 (1979).
[44] T. Kasama, N. S. Church, J. M. Feinberg, R. E. Dunin-Borkowski, and R. J. Harrison, Earth Planet. Sci. Lett. **297**, 10 (2010).
[45] G. Q. Gong, A. Gupta, G. Xiao, W. Qian, and V. P. Dravid, Phys. Rev. B **56**, 5096 (1997).
[46] W. Palmer, Phys. Rev. **131**, 1057 (1963).
[47] K. Kato and S. Iida, J. Phys. Soc. Jpn. **50**, 2844 (1981).
[48] S. Celotto, W. Eerenstein, and T. Hibma, Eur. Phys. J. B **36**, 271 (2003).